water

MDPI

Article

Stability Assessment of Reservoir Bank Anti-Dip Slopes Using a Modified Goodman–Bray Method and Monte Carlo Simulation

Junheng Chen [1], Jiawen Zhou [2,3], Nan Jiang [2,*], Haibo Li [1], Yuxiang Hu [1], Hongyu Luo [2] and Jieyuan Zhang [2]

[1] College of Water Resources and Hydropower, Sichuan University, Chengdu 610065, China; 2023223065086@stu.scu.edu.cn (J.C.); hbli@scu.edu.cn (H.L.); yxhu@scu.edu.cn (Y.H.)
[2] State Key Laboratory of Hydraulics and Mountain River Engineering, Sichuan University, Chengdu 610065, China; jwzhou@scu.edu.cn (J.Z.); hyluo@scu.edu.cn (H.L.); 2021323060054@stu.scu.edu.cn (J.Z.)
[3] Institute for Disaster Management and Reconstruction, Sichuan University-The Hong Kong Polytechnic University, Chengdu 610200, China
* Correspondence: jiangnan@scu.edu.cn

Abstract

Toppling failure is a fundamental mode of instability in rock slopes and occurs predominantly in reservoir bank anti-dip bedded rock masses. Reservoir impoundment changes seepage conditions and weakens slopes, whereas discontinuity non-persistence introduces uncertainty and complicates the identification of coupled toppling–sliding mechanisms. To address this, a probabilistic framework using the Goodman–Bray limit equilibrium method is developed. Equivalent strength parameters are introduced to unify the strength contrast between unsaturated and saturated segments along a common basal surface. Basal discontinuity connectivity is modeled as a random variable, and a Monte Carlo simulation is used to derive failure mode probabilities and a probability-weighted factor of safety. The framework is applied to the Huangcaoping anti-dip slope in the Dagangshan reservoir area at a normal water level of 1130 m. The most probable scenario has a probability of 0.116, involving sliding at 1120–1420 m and toppling at 1420–1550 m, with a probability-weighted mean factor of safety of 0.978. Predicted failure characteristics and deformation intervals are consistent with engineering observations, confirming the method's effectiveness. This integration enables the simultaneous characterization of stability levels and the evolution mechanism. The approach provides mechanism-explicit mode likelihoods and a robust stability metric to support hazard assessment, monitoring placement, and reinforcement design.

Keywords: anti-dip layered rock mass; toppling slope; reservoir water action; GB method; Monte Carlo simulation; failure-mode probability; factor of safety

Academic Editor: Mario Parise

Received: 10 January 2026
Revised: 9 February 2026
Accepted: 12 February 2026
Published: 18 February 2026

1. Introduction

Toppling failure is one of the fundamental instability modes of rock slopes, which occurs predominantly in anti-dip bedded rock slopes [1]. Its typical mechanical evolution can be described as follows: rock columns or blocks delineated by discontinuities interact and constrain one another under gravity, undergoing bending deformation toward the free face or rotating about their supporting zones, eventually leading to overturning instability [2–6]. Early engineering practice identified and systematically summarized the geometric and structural controls governing toppling in anti-dip layered slopes, which laid the foundation for subsequent mechanistic investigations and engineering diagnosis [7,8]. Subsequent classification schemes commonly distinguish three principal failure types:

sliding failure, toppling failure, and combined sliding–toppling failure. Within the toppling-related categories, several secondary modes have been proposed to capture field-scale complexities, including basal sliding-related toppling, step-path toppling, and progressive toppling [9,10].

Slope failures are commonly triggered by external factors, among which water action is widely recognized as a key control on reservoir bank slope instability [11,12]. A historical emblematic example is the 1963 Vajont landslide in Italy, where a massive rock mass slid into the reservoir, causing catastrophic casualties [13]. In recent years, with the progressive impoundment of cascade reservoirs in Southwest China, toppling deformation and toppling–sliding failures of anti-dip rock slopes along reservoir banks have become increasingly prominent [14–17]. Existing studies indicate that reservoir impoundment influences stability through multiple mechanisms. On the one hand, water softens joint surfaces and rock masses within the submerged zone, promoting evolution of the toppling mass from creep-dominated toppling toward progressive sliding [18–21]. On the other hand, rising water levels increase fissure water pressure and create internal–external pressure differentials, making the slope more prone to toppling–sliding along weak structural planes; the combined failure of toppling blocks and sliding blocks often constitutes the dominant deformation pattern [22,23]. The slope toe, particularly the adjacent anti-sliding section, is identified as the critical triggering zone for the onset of movement. Reservoir impoundment and rainfall-driven recharge tend to focus seepage within the toe fracture network, promoting pore pressure build-up, reduced effective normal stress, and localized shear softening. This toe damage can be further enhanced by erosion and hydraulic weakening, producing a cantilever-like response and a coupled flexural–shear mechanism under self-weight and overburden loads. Once initiated, toe failure may generate an upward traction effect that propagates coupled shear–toppling deformation upslope and links with rear-edge tensile cracking, ultimately leading to global instability [24–26].

Owing to their computational efficiency, intuitive outputs, and clear mechanical interpretability, numerical analytical approaches have been extensively employed to investigate toppling failure in anti-dip bedded rock masses [27–31]. These approaches, grounded in block kinematics and static or dynamic equilibrium, can explicitly represent sliding along discontinuities, rotation about a toppling point, and coupled sliding–rotation processes. By avoiding the need to solve continuum stress fields, they enable geometric characteristics and key inputs—such as discontinuity shear and tensile strengths and water pressure—to be introduced explicitly, thereby supporting efficient assessment of structurally controlled stability. Within this family of analytical frameworks, limit equilibrium block-based methods constitute the most fundamental class. Among these methods, the most widely used is the Goodman–Bray toppling stability analysis method [1], hereafter referred to as the GB method. The potential toppling mass is discretized into a set of slices/blocks according to their bedding or jointing, and the failure surface is idealized as step-like while satisfying static equilibrium. Stability, toppling, or sliding is then evaluated through force and moment equilibria for each block. A top-down recursive procedure is often adopted to transmit interlayer interaction forces to the slope toe. The overall stability is judged according to whether an additional external force is required to maintain equilibrium of the toe block, yielding a systematic and readily implementable calculation procedure for engineering applications. Subsequent studies have continually refined the assumptions on block discretization, the identification of failure modes, and the consideration of external actions, further enhancing the practical applicability of these methods [32–34]. In addition to mechanics-based stability assessment approaches, monitoring-driven prediction methods have been developed using pre-failure surface tilting and movement-rate time histories for landslide early warning [35,36]; related work has also emphasized the progressive evo-

https://doi.org/10.3390/w18040505

lution of failure depth under strong engineering disturbances, suggesting that subsurface failure development can be an important complement to surface-based indicators [37].

Although some GB-based formulations incorporate reservoir water effects, they typically do so by considering hydrostatic pressures between adjacent rock columns, together with reservoir water pressure [38]. Two common limitations are as follows: (i) strength degradation is often imposed empirically and may not adequately reflect seepage-induced pore pressure weakening of shear resistance; and (ii) discontinuity persistence and connectivity are frequently treated as deterministic or spatially uniform, failing to represent the strong spatial variability inherent in natural rock masses.

To address these limitations, this study develops a mechanistic–probabilistic enhancement to the factor of safety evaluation for reservoir bank anti-dip toppling slopes. For limitation (i)—namely, the largely empirical treatment of strength degradation that may not adequately represent seepage-induced pore pressure weakening—we introduce equivalent strength parameters directly into the mechanical formulation such that pore pressure effects are incorporated in a physically consistent manner. For limitation (ii)—namely, the deterministic or spatially uniform representation of discontinuity persistence or connectivity that fails to capture the pronounced heterogeneity of natural rock masses—we adopt Monte Carlo simulation to explicitly model the randomness of connectivity and propagate its uncertainty into the FoS calculation.

Building on this foundation, we further advance the GB method in three key ways. First, the governing failure mode is no longer selected based on a deterministic extremum criterion; instead, the set of GB-enumerated failure modes is extended to a Monte Carlo-based probabilistic identification of the controlling mode, enabling direct quantification of mode likelihood under uncertainty. Second, we introduce two parallel sensitivity analysis pathways: a fixed-reference scheme to ensure strict comparability across parameter perturbations and a parameter-varying scheme to preserve physical realism as parameters evolve. Third, using common random samples for controlled comparisons, back-calculating FoS, and reporting a weighted FoS, we establish a unified statistical framework that simultaneously supports stability assessment and the probabilistic characterization of failure mechanism evolution.

2. Study Area

2.1. Engineering Geology

Huangcaoping Deformation Mass is located in Xinhua Village, Detuo Town, Luding County, Sichuan Province, on the left bank of the Dagangshan Reservoir along the Dadu River. The site lies approximately 16.8 km upstream of the dam location, as shown in Figure 1a. The strata are dominated by thin-bedded sandstone and shale of the Triassic Baiguowan Formation, locally intercalated with gneiss and other lithologies. The bedding steeply dips out of the slope and intersects the bank slope strike at a small angle. Following the Phase II reservoir impoundment in 2015, tensile cracking developed along the rear margin of the slope mass. Deformation has intensified since August 2016, accompanied by localized collapses in the middle-to-front portion, indicating poor overall stability. The deformation mass exhibits a structurally controlled, “armchair-shaped” irregular elliptical planform, with an along-river length of 700 m, a width of 680 m, and a total relief of 485 m. Based on field investigations, the Huangcaoping deformation mass can be divided into three regions, including Region I (strongly deformed region), Region II (moderately deformed region), and Region III (slightly deformed region), as shown in Figure 1b.

https://doi.org/10.3390/w18040505

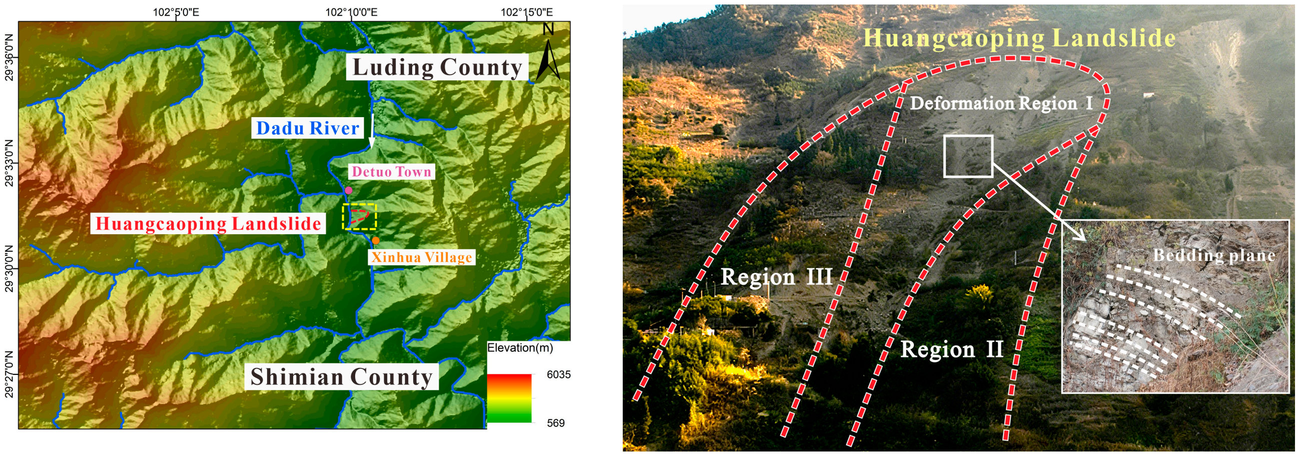

(a) (b)

Figure 1. Location, topography, and field zonation of the Huangcaoping landslide. (**a**) Schematic map showing the location and topography. (**b**) Field photograph showing the zonation.

The exposed lithologies mainly include Jinningian granodioritic gneiss, Chengjiangian biotite monzogranite, sandstone and shale of the Triassic Baiguowan Formation, and Quaternary cover deposits. The deformation mass is composed predominantly of thin-bedded sandstone and shale of the Triassic Baiguowan Formation. The bedding dips steeply toward the northwest, with angles ranging from 67° to 85°. The bedding strike intersects the river valley slope at a small angle. The intersection angle between the bedding strike and the bank slope strike is about 10°, and the strata dip steeply out of the slope. Based on the field geological survey, the geological profile of Deformation Region I is shown in Figure 2. The mass can be divided into three zones: Zone A (extremely intense toppling), where dense tensile cracking and pronounced rock mass loosening occur in the near-surface layer; Zone B (intense toppling), characterized by evident intra-bed shear sliding and cross-bed propagation; and Zone C (weak toppling), where only minor microcracks are observed, as shown in Figure 2. As a loose accumulation composed of colluvial–proluvial gravelly soil and strongly toppled rock masses, the deformation body currently exhibits creep-related sliding–tension cracking and localized instability under the combined triggering effects of reservoir impoundment and rainfall. The Huangcaoping deformation mass is primarily composed of a colluvial deposit consisting of blocky gravelly soil, locally involving the fractured/loosened zone and rock masses within the strong toppling zone. Under adverse factors such as reservoir level fluctuations and precipitation, the slope has developed creep-driven sliding accompanied by tensile cracking, with intermittent localized failures.

To compensate for the lack of early-stage impoundment monitoring, SBAS-InSAR was applied to 121 Sentinel-1 IW descending images (Figure 3) to derive a deformation time series. The Huangcaoping mass trends north–south and faces west, with motion dominated by downslope (approximately westward) sliding. As a single descending track measures only LOS displacement, the observed deformation represents the LOS projection of this westward motion, making the slope deformation detectable as a persistent evolution of LOS displacement. Negative values represent LOS displacement away from the satellite, corresponding to downslope motion along the slope aspect for this viewing geometry.

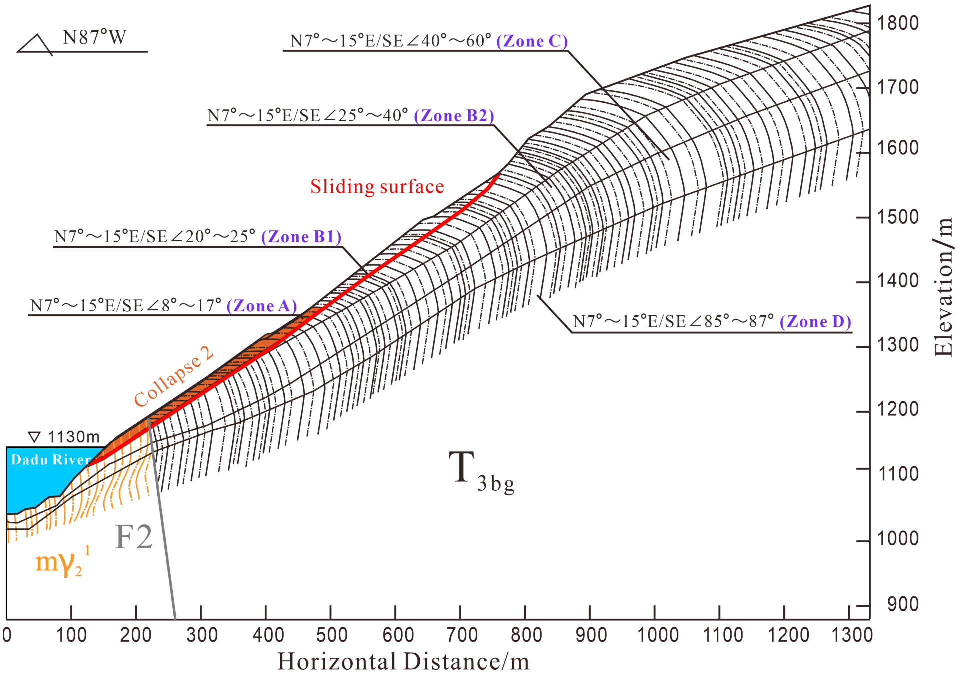

Figure 2. Toppling deformation characteristics of the Huangcaoping deformation mass: Jinningian tonalitic gneiss ($m\gamma_2^1$); fracture 2 (F2); and sandy shale (T_{3bg}).

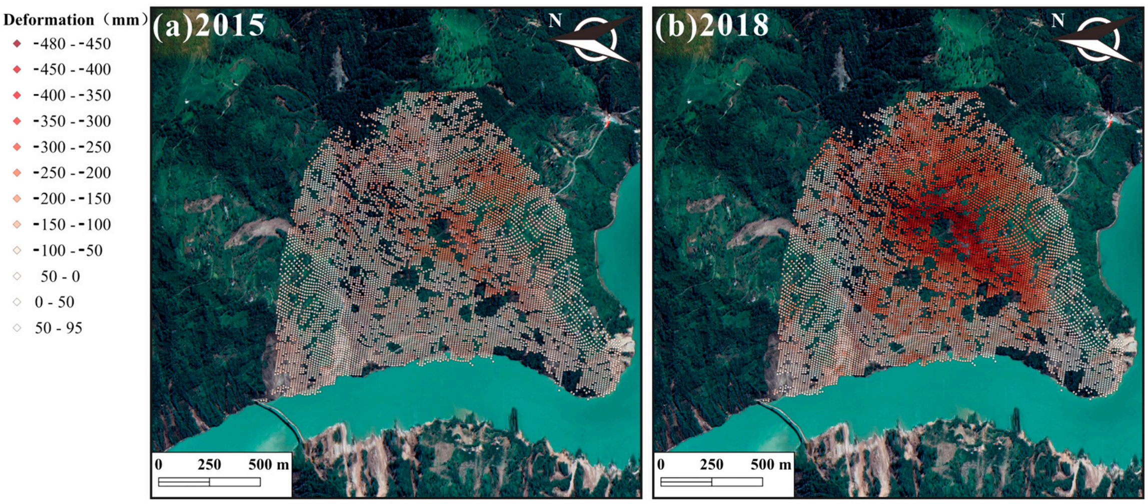

Figure 3. Cumulative displacement cloud map from InSAR monitoring. (**a**) 2015. (**b**) 2018.

2.2. Hydrological Condition

The impoundment process of the Dagangshan Hydropower Station can be summarized as follows. On 30 December 2014, the left-bank diversion tunnel gate was closed, and the reservoir water level rose to approximately 1005 m in the first impoundment stage. On 29 May 2015, the diversion bottom outlet was closed, marking the start of the second stage. The reservoir reached the dead water level of 1120.00 m on 4 July 2015. The first generating unit was officially connected to the grid and entered commercial operation on 2 September 2015. The reservoir was impounded to the normal water level of 1130.00 m for the first time on 29 October 2015. The impoundment history is shown in Figure 4.

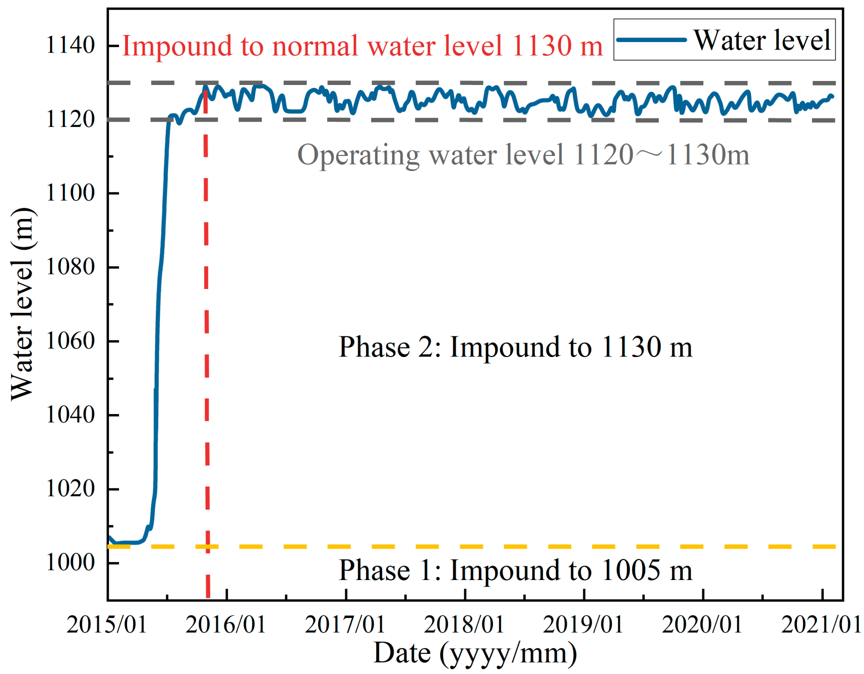

Figure 4. Impoundment history of the Dagangshan Reservoir.

3. Methodology

The GB method divides the potential toppling mass into bedding parallel blocks and evaluates equilibrium by propagating interlayer forces from crest to toe [1]. Zhang extended the GB by introducing an explicit factor of safety through combined shear–tensile strength reduction and applying Sarma's concept to identify the governing failure mode during FoS iteration [10]. Subsequent extensions introduce a connectivity ratio and generalized block geometries to better represent rock bridges and complex discontinuity–geometry effects, as well as hydrostatic pressures between adjacent rock columns and reservoir water pressure [38]. The present study builds upon these previous studies.

3.1. GB-Based Improved Reservoir Area Toppling Assessment

Following this framework, a geological model for an anti-dip slope under reservoir impoundment is established, as shown in Figure 5. Blocks/slices are numbered from the slope toe upward. The indices of the last sliding block and last toppling block are denoted as N_s and N_t, respectively, and the total number of blocks is N. Based on the stress distribution within rock bridges and the corresponding anti-toppling resisting moment, force equilibrium is enforced. At failure, the upstream-left endpoint of the basal surface is assumed to reach the rock-bridge tensile strength σ_t, with the rock-bridge ratio defined as $\xi = 1 - k$. In the strength reduction process, the shear strength parameters c and $\tan\varphi$ and the tensile strength σ_t are reduced consistently. For numerical implementation, Sarma's procedure is adopted by first computing the critical acceleration: a horizontal pseudo-static force $\eta\,\Delta W$ is applied to each block, where η is the critical acceleration coefficient and ΔW is the block weight. The FoS, F, is defined as the reduction factor applied to c, $\tan\varphi$, and σ_t, such that the corresponding critical acceleration coefficient satisfies $\eta = 0$.

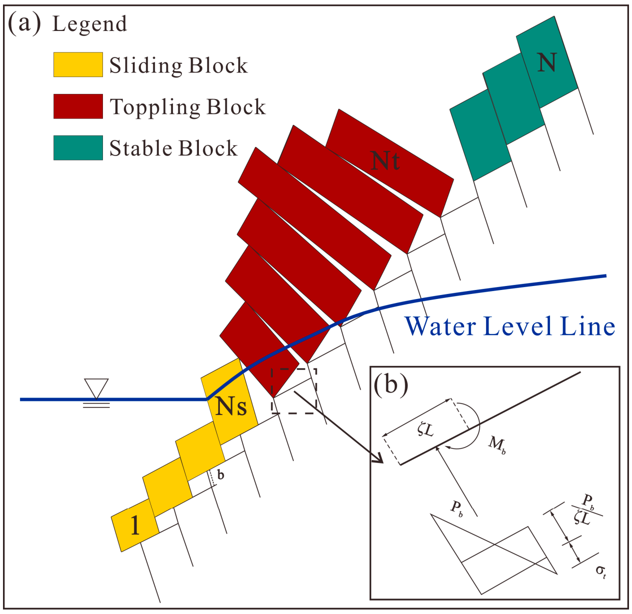

Figure 5. Schematic diagram of the computational procedure for the modified GB method: (**a**) failure modes of an anti-dip slope under reservoir impoundment conditions; (**b**) force analysis of the rock bridge.

The discontinuity persistence ratio k is treated as a random variable that is assumed to follow a normal distribution; that is, $k \sim N(\mu, \sigma^2)$. Monte Carlo sampling is employed to generate realizations of k, which are then substituted into the mechanical model. By counting the occurrence frequency of each toppling failure mode under different combinations, a probabilistic distribution of failure modes is obtained. The factor of safety for each mode is further evaluated, and an occurrence- and probability-weighted factor of safety is calculated to yield an equivalent factor of safety that reflects the overall risk of instability.

Reservoir impoundment saturates the rock mass and joints, leading to pronounced degradation of shear strength. In the Goodman–Bray (GB) limit equilibrium framework, the rock mass is idealized as a rigid block undergoing overall motion. When a single potential sliding surface includes both subaerial and submerged segments, the GB recursive solution requires the mixed condition to be represented by a unified set of equivalent parameters such that one stability index can be applied to the whole block. Cohesion, reflecting material bonding, is commonly treated as independent of normal stress; thus, for partial submergence, the equivalent cohesion is taken as an area-weighted combination of the subaerial and submerged portions. Frictional resistance depends on the effective normal stress on the sliding surface. Following the effective stress principle, only effective stress contributes to shear resistance. Therefore, reservoir-level fluctuations modify uplift pressure, which directly alters effective normal stress and is reflected as a corresponding reduction or increase in frictional resistance. To simultaneously account for the unsaturated and saturated segments on the same contact surface, an equivalent cohesion c and an equivalent friction angle φ are introduced, and the equivalent shear strength parameters for both block side surfaces and basal surfaces are derived accordingly. Let the total contact area be D, with the natural segment area D' and the saturated segment area $D_s = D - D'$. The shear strength parameters of the natural segment are (c_d, φ_d), whereas those of the saturated segment are $(c_{\text{sat}}, \varphi_{\text{sat}})$.

The equivalent cohesion is defined as an area-weighted average over the contact surface:

$$c = \frac{D' c_d + (D - D') c_{sat}}{D} \quad (1)$$

In deriving the equivalent friction term, σ_n denotes the total normal stress acting on the contact surface. Here, $\sigma_{n,d}$ denotes the total normal stress on the natural segment, and $\sigma_{n,\mathrm{sat}}$ denotes the total normal stress on the saturated segment. In addition, α_b is the Biot coefficient. Here, u_{sat} is the pore water pressure on the saturated segment and is typically calculated from the hydraulic head. The total normal stress is decomposed as follows:

$$\sigma_n = \sigma_d + \sigma_{sat} \tag{2}$$

The effective stress principle is introduced. The effect of pore water pressure is incorporated by replacing total normal stress with effective normal stress. The effective normal stress on the saturated segment is expressed as follows:

$$\sigma_{sat} = \sigma_{n,sat} - \alpha_b u_{sat} \tag{3}$$

Accordingly, the normal forces carried by the natural and saturated segments are written as follows:

$$N_d = \sigma_d D', N_{sat} = \sigma_{sat} D_s \tag{4}$$

The equivalent friction coefficient is defined as follows:

$$tan\varphi = \frac{N_d\ tan\varphi_d + N_{sat}\ tan\varphi_{sat}}{N_d + N_{sat}} \tag{5}$$

In the recursive calculation of inter-slice forces, this study departs from the top-down scheme of the Goodman–Bray method and instead adopts a reverse recursion from the slope toe to the slope crest. The forces acting on the sliding and toppling blocks are shown in Figure 6. By performing a force equilibrium analysis for an individual block, the following recurrence relations for inter-slice forces are derived as follows:

$$P_r = AP_l + B + \eta C \tag{6}$$

where P_r denotes the force acting on the right side of the block, P_l denotes the force acting on the left side, and A, B, and C are coefficients that can be obtained by solving the equilibrium equations for the sliding and toppling blocks.

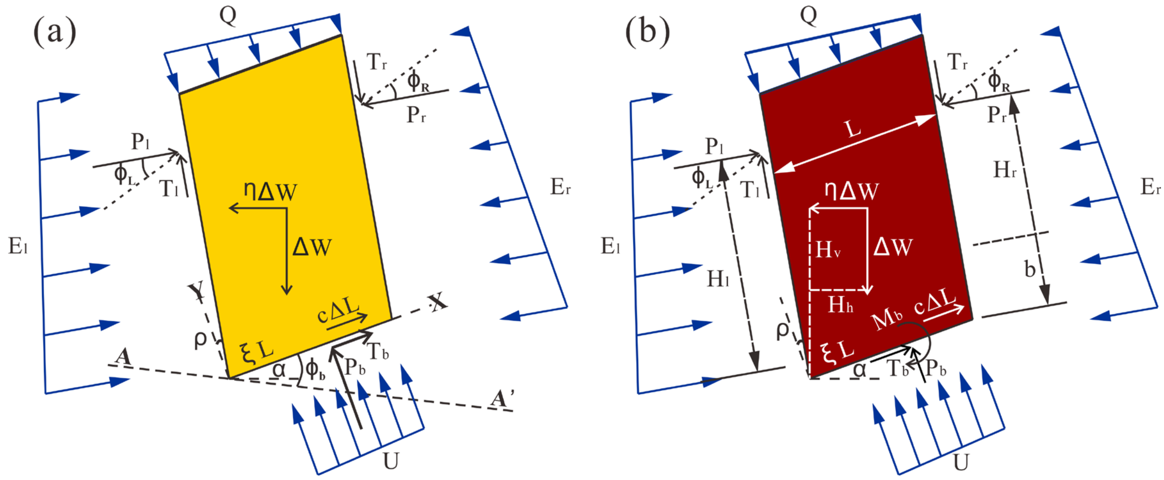

Figure 6. The forces acting on the sliding and toppling block. (**a**) Sliding block. (**b**) Toppling block.

For the derivation of the governing equations for the sliding block, the normal force on the basal sliding surface P_b and the basal friction force T_b are first combined into a resultant reaction vector S, as shown in Figure 6a. The angle between this unknown reaction S

and the normal to the basal surface equals the basal friction angle φ_b. To avoid solving directly for the unknown S, the AA' axis is defined as the projection axis and is oriented perpendicular to S, denoted as the $\perp S$ direction. All forces acting on the rock column are then projected onto this axis. Along the chosen projection direction, the component of S is zero; therefore, it is eliminated from the static equilibrium equations. The geometric angles of each force vector with respect to the x axis and the AA' axis are listed in Table 1.

Table 1. The decomposed force components of the sliding and toppling block.

Force Acting on the Rock Column	Angle Relative to the Basal Sliding Surface Direction	Angle Relative to the Positive Direction of the AA' Axis	Angle Relative to the Basal Sliding Surface Normal
Q	$\pi/2$	$\pi/2-\phi_b$	π
$P_l sec\varphi_l$	$\phi_l-\rho$	$\phi_l+\phi_b-\rho$	$\pi/2+\rho-\phi_l$
$P_r sec\varphi_r$	$\pi+\phi_r-\rho$	$\pi+\phi_r+\phi_b-\rho$	$\pi/2-\rho+\phi_r$
$\eta'\Delta W$	$\pi-\alpha$	$\pi-\alpha+\phi_b$	$\pi/2-\alpha$
ΔW	$\pi/2+\alpha$	$\pi/2+\alpha-\phi_b$	$\pi-\alpha$
$c\Delta L$	0	ϕ_b	$\pi/2$
U	$\pi/2$	$\pi/2+\phi_b$	0
E_r	$\pi-\rho$	$\pi+\phi_b-\rho$	$\pi/2-\rho$
E_l	$-\rho$	$\phi_b-\rho$	$\pi/2+\rho$

The static equilibrium equations for the sliding block are given as follows:

$$\begin{gathered} P_r sec(\varphi_r)cos(\pi+\varphi_b+\varphi_r-\rho)+P_l sec(\varphi_l)cos(\varphi_l+\varphi_b-\rho)+\ Qcos\left(\tfrac{\pi}{2}-\varphi_b\right)+\ \eta' Wcos(\pi-\alpha+\varphi_b) \\ +\ Wcos\left(\tfrac{\pi}{2}+\alpha-\varphi_b\right)+\ c\ Lcos(\varphi_b)+\ Ucos\left(\tfrac{\pi}{2}+\varphi_b\right)+E_l cos(\varphi_b-\rho)+E_r cos(\pi+\varphi_b-\rho)=\ 0 \end{gathered} \tag{7}$$

Let $K = sec\varphi_r cos(\varphi_b+\varphi_r-\rho)$. Then,

$$A=\frac{sec\varphi_l cos(\varphi_l+\varphi_b-\rho)}{K} \tag{8}$$

$$B=\frac{Wsin(\varphi_b-\alpha)+cL\ cos\varphi_b+(E_l-E_r)\,cos(\varphi_b-\rho)-U\ sin\varphi_b+Q\ sin\varphi_b}{K} \tag{9}$$

$$C=-\frac{Wcos(\varphi_b-\alpha)}{K} \tag{10}$$

For the derivation of the governing equations for the toppling block, as shown in Figure 6b, projecting the forces acting on the rock column onto the direction normal to the basal sliding surface yields the following:

$$\begin{gathered} P_b+\ Q\cos\pi+P_l\sec\varphi_l\cos\left(\tfrac{\pi}{2}-\varphi_l+\rho\right)+P_r\sec\varphi_r\cos\left(\tfrac{\pi}{2}+\varphi_r-\rho\right)+ \\ \eta W\cos\left(\tfrac{\pi}{2}-\alpha\right)+\ W\cos(\pi-\alpha)+\ U\cos 0+E_l\cos\left(\tfrac{\pi}{2}+\rho\right)+E_r\cos\left(\tfrac{\pi}{2}-\rho\right)=\ 0 \end{gathered} \tag{11}$$

A moment equilibrium equation is established for all forces about the downstream lower edge of the rock block, given as $M_b=\frac{\xi L}{6}(\sigma_t\xi L+P_b)$.

$$\begin{gathered} Q\ H_q+P_l H_l-P_r(H_r+b+L\sin\rho)-P_r\tan\varphi_r L\cos\rho-\eta W\ H_v \\ -W\ H_h+M_b-\tfrac{\xi L P_b}{2}-H_u U+E_l H_{el}-E_r H_{er}=0 \end{gathered} \tag{12}$$

Solving the equations simultaneously, the coefficients for each variable are obtained as follows:

$$K=H_r+b+L\ sin\rho-L\ tan\varphi_r\ cos\rho+\frac{\xi L}{3}sec\varphi_r\sin(\varphi_r-\rho) \tag{13}$$

$$A=\frac{1}{K}\left[H_l+\frac{\xi L}{3}sec\varphi_l\ \sin(\varphi_l-\rho)\right] \tag{14}$$

$$B = \frac{1}{K}\left[Q\left(H_q - \frac{\xi L}{3}\right) - W\left(H_h + \frac{\xi L\ cos\alpha}{3}\right) + U\left(\frac{\xi L}{3} - H_u\right) + \frac{(\xi L)^2\sigma_t}{6} + E_l H_{el} - E_r H_{er} - \frac{\xi L}{3}(E_l - E_r)\ sin\rho\right] \tag{15}$$

$$C = \frac{1}{K}\left[\frac{\xi L W sin\alpha}{3} - W H_v\right] \tag{16}$$

To clearly elucidate the mechanisms by which reservoir water-level fluctuations influence the stability of anti-dip slopes, this study develops, within an improved limit equilibrium framework, a computational chain that links hydraulic boundary conditions directly to the stability factor. The procedure is shown in Figure 7.

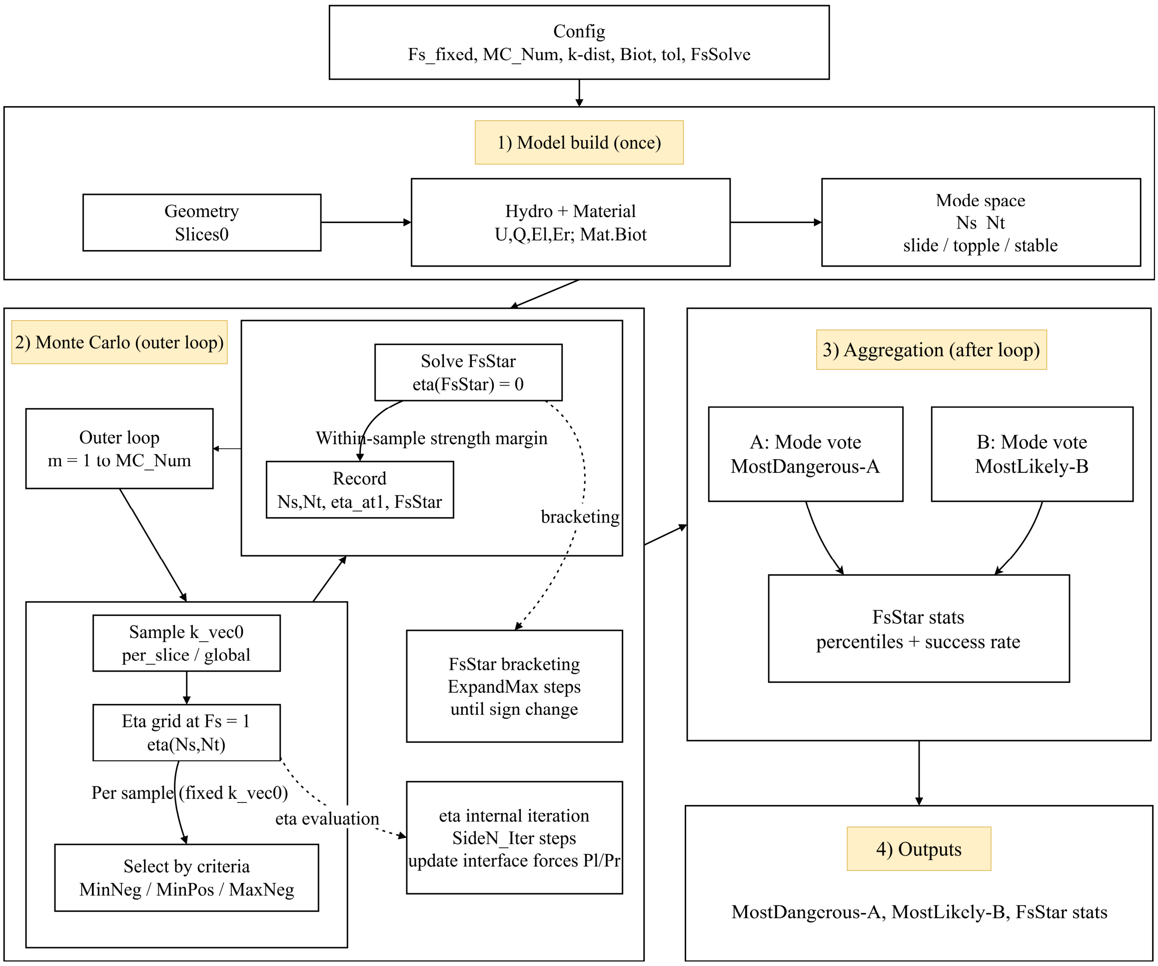

Figure 7. Workflow of the improved GB method.

3.2. Criteria for Governing Failure Mode Identification

The improved GB method requires an exhaustive search over a large number of candidate failure modes, represented by the (N_s, N_t) combinations. Without a robust screening criterion, it is difficult to identify a governing mechanism with clear physical meaning. Moreover, the subsequent factor of safety computation, denoted by F_s, may fail to converge because of mode switching during the iteration. To address this issue, a threshold η_{tol} is introduced to delineate the stable domain $\Omega_+ = \{(N_s, N_t)|\eta > +\eta_{\text{tol}}\}$ and the unstable domain $\Omega_- = \{(N_s, N_t)|\eta < -\eta_{\text{tol}}\}$. A comparative analysis is subsequently conducted to examine the physical interpretation and applicability of three commonly used criteria.

3.2.1. MinNeg Criterion: The Minimum Negative Value Rule

When the system has entered an unstable state (i.e., $\Omega_- \neq \varnothing$), the failure mode with the smallest value of η—that is, the most negative η—is selected from the unstable domain Ω_- as follows:

$$\eta_{\text{MinNeg}} = \min\{\eta | \eta \in \Omega_-\} \tag{17}$$

A smaller negative value of η indicates that the system is farther from equilibrium, meaning that the unbalanced force, or the downslope driving potential, is greatest for that mode. In practical engineering applications and numerical analyses, the MinNeg criterion often identifies local, small-scale failure modes, such as sliding or toppling of a limited number of blocks. This tendency is not necessarily a drawback. It is consistent with field observations for many slopes, where large-scale global collapse commonly evolves progressively from localized damage, localized weakening, or progressive coalescence of discontinuities.

3.2.2. MaxNeg Criterion: The Maximum Negative Value Rule

Within the unstable domain Ω_-, this criterion selects the mode with a negative η value closest to zero as follows:

$$\eta_{MaxNeg} = \max\{\eta | \eta \in \Omega_-\} \tag{18}$$

MaxNeg captures a critical state that has just crossed the limit equilibrium boundary. Compared with cases where η may be dominated by extreme local instabilities, MaxNeg is more consistent with a realistic global failure path. During the iterative back-calculation of the critical factor of safety F_s, this criterion tends to provide a more stable and continuous indicator and can effectively reduce the influence of numerical singularities on root finding. Therefore, MaxNeg is preferred for identifying the critical state and for back-calculating F_s.

3.2.3. MinPos Criterion: The Minimum Positive Value Rule

When the system remains globally stable, this criterion selects, from the stable domain Ω_+, the mode with the positive η value closest to zero as follows:

$$\eta_{MinPos} = \min\{\eta | \eta \in \Omega_+\} \tag{19}$$

MinPos represents the smallest stability margin under stable conditions. A smaller positive η indicates that only a minor perturbation is required to break the equilibrium. The corresponding mode is therefore identified as the current potential failure mode.

4. Results

4.1. Model Setup and Calculation Scheme

The computational model covers the slope over an elevation range of 1100–1540 m. The analysis domain is focused primarily on Zone A, the extremely intense toppling zone, as shown in Figure 8. For the analysis, the slope mass was discretized into 30 blocks from bottom to top in MATLAB R2022b. Based on the investigation report and laboratory physical tests [39], the input parameters were determined as listed in Table 2, including gravitational acceleration and unit weight of water, together with a saturation reduction factor to account for strength degradation under wetting conditions. The shear strength parameters follow the Mohr–Coulomb criterion and are specified for both the side surface and the base surface. Moreover, the tensile strength was also considered [20]. In addition, the main lithologies in the study area, such as gneiss and sandy shale, were assigned cohesion and friction angle values accordingly. To incorporate uncertainty, the connectivity parameter was treated statistically and evaluated using Monte Carlo sampling, and the Biot effective stress coefficient was adopted for effective stress calculations.

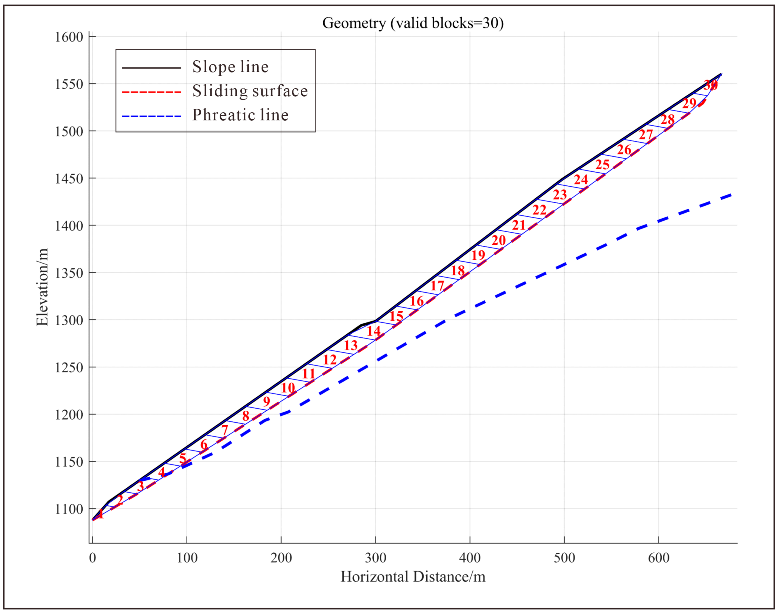

Figure 8. Schematic diagram for the stability analysis.

Table 2. The mechanical parameters of the slope.

Symbol	Engineering Meaning	Unit	Baseline Value
g	Gravitational acceleration	m/s^2	9.81
γ_w	Unit weight of water	kN/m^3	9.81
r_{sat}	Saturation reduction	–	0.7
φ_s	Side friction angle	deg	25
c_s	Side cohesion	kPa	75
φ_b	Base friction angle	deg	23
c_b	Base cohesion	kPa	100
σ_t	Tensile strength	kPa	100
c_g	Gneiss cohesion	kPa	400
φ_g	Gneiss friction angle	deg	24
c_s	Sandy shale cohesion	kPa	500
φ_{ss}	Sandy shale friction angle	deg	26
μ_k	Mean of connectivity parameter k	–	0.7
σ_k	Std. dev. of connectivity parameter k	–	0.1
M	Monte Carlo sample count per parameter value	–	1000
α_B	Biot effective stress coefficient	–	0.8

4.2. Failure Mode Probability and Classification

Using the MaxNeg criterion, the (N_s, N_t) failure modes obtained from a total of 1000 Monte Carlo simulations are summarized in Table 3. In this study, only failure modes with more than 10 occurrences were retained for statistical reporting. Because the persistence ratio k is treated as an uncertain variable with a probabilistic distribution, each random realization yields a selected governing mode. As a result, under the same parameter condition, multiple failure modes can coexist, each associated with a distinct occurrence probability.

Table 3. Failure modes and corresponding frequencies.

Ns	Nt	Counts	Probability
23	30	116	0.116
20	25	97	0.097
11	16	90	0.09
12	17	85	0.085
10	14	84	0.084
13	18	83	0.083
22	28	73	0.073
23	29	70	0.07
9	13	44	0.044
5	8	43	0.043
21	26	38	0.038
3	5	30	0.03
10	15	29	0.029
2	3	22	0.022
19	24	19	0.019
8	12	17	0.017
7	11	15	0.015
6	10	11	0.011

The probability distribution indicates that the most likely failure mode is (23, 30), with a probability of $p = 0.116$. The second most likely mode is (20, 25), with $p = 0.097$. Modes such as (11, 16), (12, 17), (10, 14), and (13, 18) exhibit probabilities clustered in the range 0.083–0.090. Even the highest frequency mode accounts for only 11.7%, indicating that no single mechanism is overwhelmingly dominant. Under Monte Carlo simulation, switching among failure modes is therefore a general feature rather than an occasional outcome.

According to the failure scale reflected by N_s and N_t, the modes can be grouped into three categories. First, the slope-spanning type accounts for approximately 41.4%. In this category, the sliding segment extends upward from the slope toe to higher elevations, and the toppling influence approaches the slope crest, representing a globally connected instability governed by sliding–toppling coupling. Second, the mid-to-lower local type accounts for about 41.2%. Sliding and toppling mainly affect the middle and lower parts of the slope, whereas the upper part remains stable, indicating that parameter uncertainty can markedly alter the governing failure scale. Its occurrence frequency is comparable to that of the slope-spanning type. Third, the shallow toe type accounts for approximately 14.1%. Failure is concentrated in a limited number of blocks near the slope toe. Although less frequent, this pattern suggests that the toe may act as an initiation zone for precursor or progressive failure, providing insight into subsequent instability evolution.

A comparative analysis is conducted by selecting the most probable failure modes identified using the MinNeg and MaxNeg criteria. The failure mode associated with MinNeg is unique and corresponds to the (1, 2) mode, as shown in Figure 9. Its failure characteristics are locally controlled. This indicates that under reservoir impoundment conditions, the toe blocks are prone to becoming unstable first because of reservoir water action and shear strength degradation. This agrees with field observations at the Huangcaoping deformation mass. Prior to impoundment at the Dagangshan Hydropower Station, no significant deformation or failure was reported. Following the first impoundment in July 2015 and the rise to the normal water level of 1130 m in October 2015, localized sliding collapses developed at the front margin of the slope.

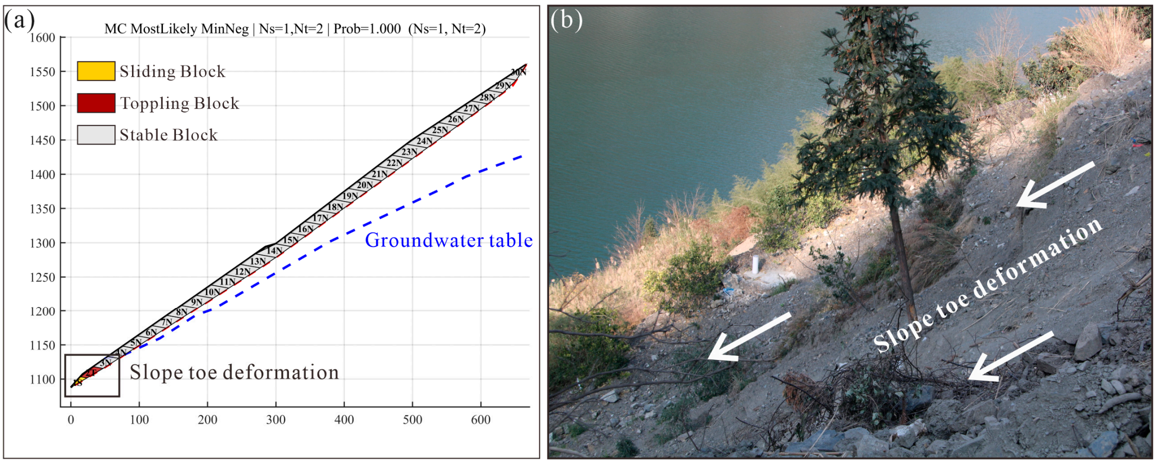

Figure 9. Failure mode determined using the MinNeg criterion. Results calculated using (**a**) the improved GB method and (**b**) toe sliding.

The most probable failure mode determined using MaxNeg is (23, 30), shown in Figure 10. The corresponding probability-weighted mean factor of safety is 0.978, indicating that the slope is in an unbalanced, near-critical state with a potential for instability. This is consistent with the extensive cracking observed in the middle part and rear margin of the deformation body after the Phase II impoundment. In terms of failure characteristics, the slope tends to undergo coupled sliding–toppling after impoundment, with sliding dominating the lower part and toppling dominating the upper part, thereby forming a continuous global instability path. The model results suggest that the sliding blocks are mainly distributed over elevations of approximately 1120–1420 m. Correspondingly, on 2 July 2018, a failure event with a volume of approximately 50,000 m^3 occurred at elevations of approximately 1120–1350 m. These comparisons indicate that the improved model effectively evaluated the stability of anti-dip rock slopes induced by reservoir impoundment, with the computed results showing good agreement with engineering observations.

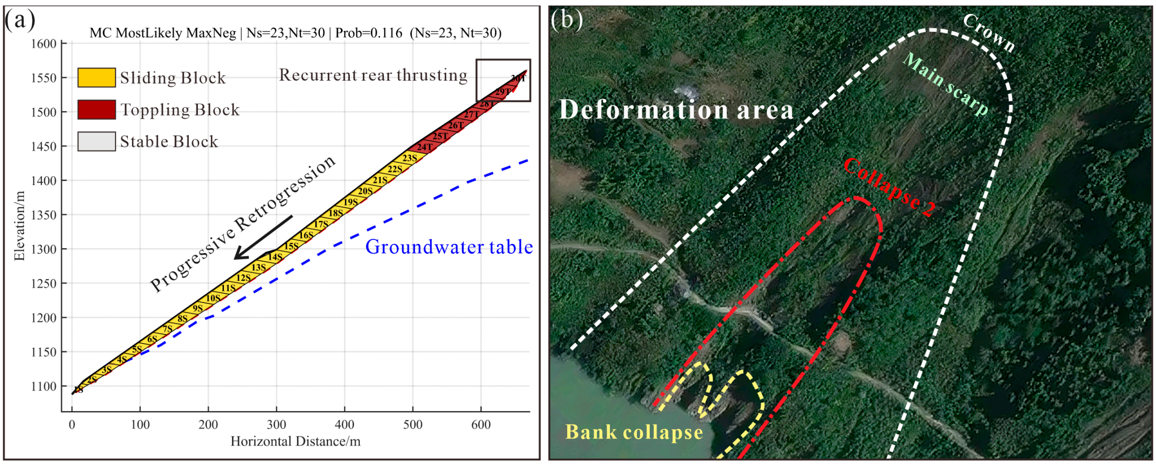

Figure 10. Failure mode determined using the MaxNeg criterion. Results calculated using (**a**) the improved GB method and (**b**) collapse 2 (2018).

4.3. Sensitivity of the Factor of Safety to Key Parameters

This study performs a sensitivity analysis on key parameters that strongly affect overall slope stability. These parameters include the discontinuity connectivity ratio, the softening coefficient, the basal shear strength, the bedding dip angle, and the tensile strength of the rock mass. Variations in these parameters not only change the stability level but may also induce transitions in the governing failure mode. As different modes correspond to different criteria and controlling conditions, their factors of safety are not directly comparable.

To ensure comparability, the failure mode of the baseline case is fixed when comparing factors of safety, and the factor of safety under each parameter setting is calculated on this basis. Meanwhile, the distribution of failure modes caused by parameter perturbations is recorded to provide an integrated understanding of how parameter changes influence both stability and the instability mechanism. The parameters used in the sensitivity analysis are listed in Table 4.

Table 4. Sensitivity analysis parameters.

Parameter Description	Symbol	Unit	Scan Values
Discontinuity connectivity ratio	k	–	0.50, 0.60, 0.70, 0.80, 0.90
Softening coefficient	r_{sat}	–	0.50, 0.60, 0.70, 0.80, 0.90
Bedding dip angle	β	deg	30, 25, 20, 15, 10
Base friction angle	φ_b	deg	18, 21, 23, 27, 32
Base cohesion	c_b	kPa	50, 80, 100, 150, 200
Tensile strength	σ_t	kPa	30, 60, 100, 200, 300

As shown in Figure 11, a sensitivity analysis is performed for the discontinuity connectivity ratio, the softening coefficient, the bedding dip angle, the basal friction angle, the basal cohesion, and the tensile strength of the rock mass. The corresponding effects on the factor of safety F_s are summarized as follows.

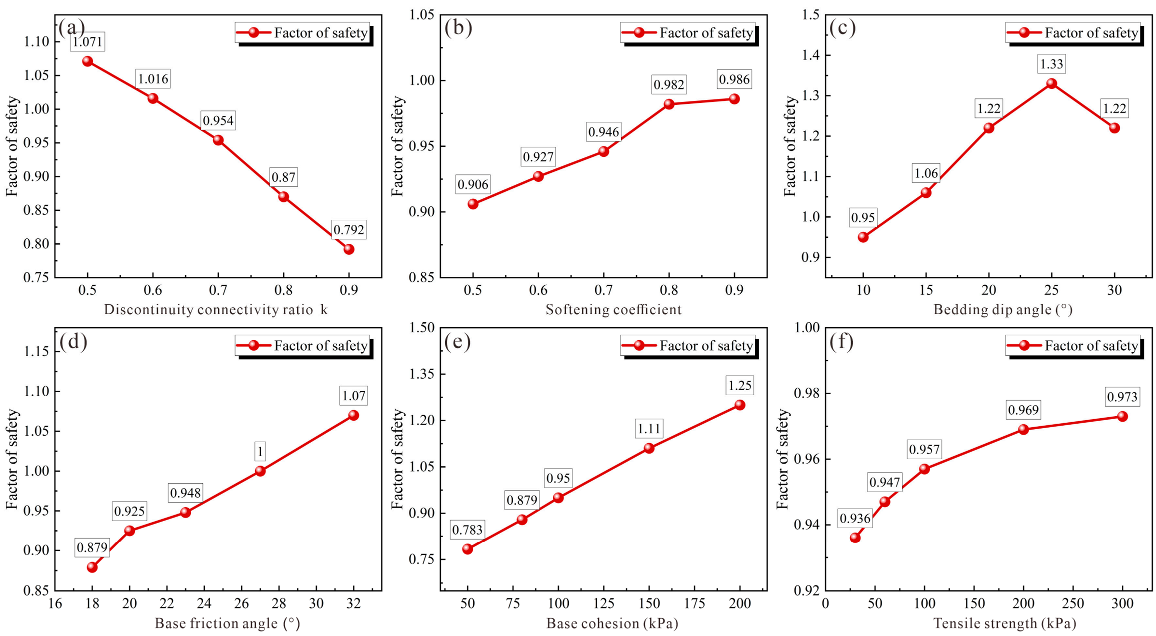

Figure 11. Sensitivity of the factor of safety F_s to key parameters: (**a**) discontinuity connectivity ratio k; (**b**) softening coefficient r_{sat}; (**c**) bedding dip angle β; (**d**) basal friction angle φ_b; (**e**) basal cohesion c_b; and (**f**) tensile strength σ_t.

(a) The basal discontinuity connectivity ratio k characterizes the degree of persistence of the potential sliding surface. As k increases, F_s decreases markedly and monotonically, dropping from 1.071 at $k = 0.5$ to 0.792 at $k = 0.9$. This indicates that higher persistence facilitates the formation of continuous sliding or toppling pathways, thereby reducing the overall resistance to shear and overturning.

(b) The softening coefficient r_{sat} describes the strength degradation in the saturated zone. With increasing r_{sat}, F_s shows a slight increase with an overall mild variation. This behavior is mainly because the softened saturated range is limited in this case, with only three blocks below the waterline. Thus, its influence on global stability remains small.

(c) The influence of the bedding dip angle β on F_s is non-monotonic. When β increases from 10° to 25°, F_s rises from 0.95 to 1.33. As β further increases to 30°, F_s decreases to 1.22. This reflects the competing effects of dip angle changes on both block geometry and force decomposition. One effect promotes shear connectivity along the slope, whereas the other enhances toppling tendency through a cantilever-like response in the upper part.

(d) Increasing the basal friction angle φ_b leads to a consistent increase in F_s from 0.879 at 18° to 1.07 at 32°. This trend highlights the stabilizing role of enhanced frictional resistance for modes governed primarily by basal shear.

(e) The basal cohesion c_b shows the highest sensitivity. As c_b increases from 50 kPa to 200 kPa, F_s rises substantially from 0.783 to 1.25. This indicates that cohesion, as the constant component of shear strength, provides pronounced reinforcement, especially in segments with low normal stress and along the controlling sliding zone.

(f) Increasing the tensile strength of the rock mass σ_t produces only a modest increase in F_s, approaching a stable level, from about 0.936 to 0.973. This suggests that, under the fixed baseline failure mode assumption, tensile failure is not governing, and the contribution of tensile strength to the global factor of safety is limited.

Considering the magnitude of variation in F_s over the investigated ranges of each parameter, the sensitivity of the factor of safety decreases in the following order:

$$c_b > \beta > k > \varphi_b > r_{\text{sat}} > \sigma_t.$$

Overall, parameters that directly control basal shear strength, including c_b and φ_b, and parameters that markedly modify geometric and kinematic conditions, including the bedding dip angle β and the connectivity ratio k, exert more pronounced effects on stability. By contrast, material softening and tensile strength contribute relatively little to the global factor of safety F_s.

4.4. UDEC Numerical Simulation for Validation

Many researchers have investigated landslides using numerical simulations [40,41]. The two-dimensional distinct-element code UDEC 7.0 has been extensively validated and applied across geotechnical and mining engineering. It is particularly well suited to modeling rockslides and slope stability problems dominated by discontinuities [42,43].

4.4.1. Model Setup

1. Geometric modeling. For supplementary numerical validation, a 2D UDEC model was developed with the same geometry and rock mass structure as the prototype slope. The model represents Deformation Region I of the Huangcaoping slope (Figure 2), spanning ~1000 m horizontally and ~800 m in elevation. Stratification and transverse joints were included. To capture the partitioned toppling structure, each zone used the mean bedding dip of that partition. Bedding dips for Zones A, B1, B2, C, and D were set to 10°, 20°, 40°, 60°, and 85°, respectively. For computational efficiency, the block aspect ratio (length/thickness) was limited to 2. Blocks were discretized with the brick command, with thicknesses of 6 m (Zone A), 12 m (Zone B1), 12 m (Zone B2), 15 m (Zone C), and 20 m (Zone D), as shown in Figure 12.
2. Parameter assignment. Assuming that slope stability is primarily controlled by jointed blocks, the blocks were represented using an elastoplastic Mohr–Coulomb model. The rock mass properties adopted in the UDEC model are summarized in Table 5

(block values) and were adjusted within ranges constrained by laboratory testing and geological investigation data [39]. Discontinuities were modeled using a Coulomb slip joint model. The joint mechanical parameters are listed in Table 6 (joints values) and were determined based on engineering analogy and previous calibration experience [20]. In addition, the strength parameters of discontinuities within the saturated zone were reduced by the softening factor to represent wetting-induced weakening.

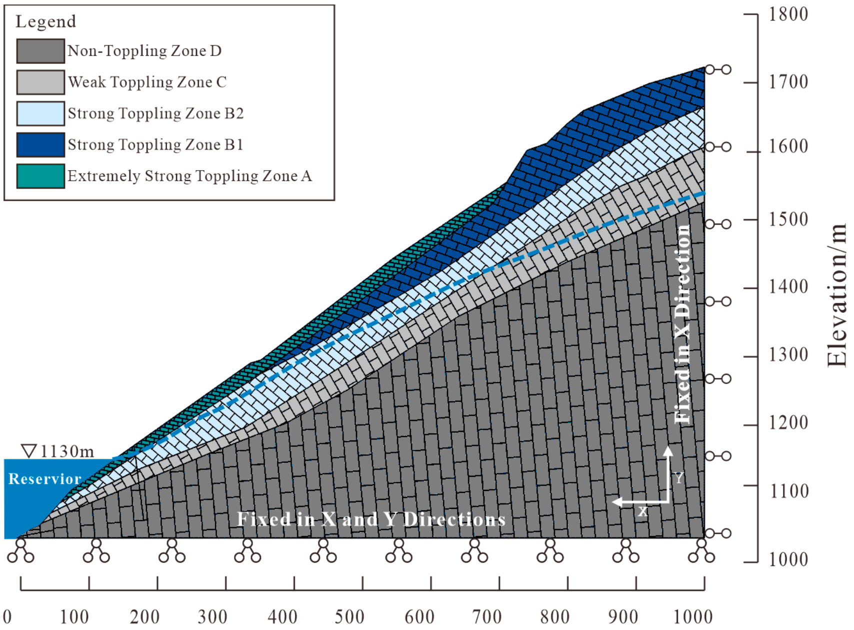

Figure 12. Discrete element numerical simulation model.

Table 5. Geotechnical parameters of rock and soil masses.

Lithology	Toppling Zone	Dry Density (kg/m^3)	Saturated Density (kg/m^3)	Dry Cohesion (MPa)	Dry Friction Angle (°)	Saturated Cohesion (MPa)	Dry Friction Angle (°)	Shear Modulus (GPa)	Bulk Modulus (GPa)
Sandstone–shale	Extremely Strong Toppling (Zone A)	2000	2100	0.03	26	0.028	24	0.08	0.13
	Strong Toppling (Zone B1)	2500	2600	0.20	30	0.19	28	0.14	0.23
	Strong Toppling (Zone B2)	2600	2650	0.30	32	0.29	30	0.20	0.33
	Weak Toppling (Zone C)	2600	2650	0.50	35	0.43	33	0.60	1.00
	Intact Rock (Zone D)	2650	2650	1.00	50	0.95	48	6.60	11.00
Gneiss	Extremely Strong Toppling (Zone A)	2000	2100	0.04	22	0.03	20	0.04	0.11
	Strong Toppling (Zone B1)	2200	2250	0.16	24.5	0.12	23	0.10	0.20
	Strong Toppling (Zone B2)	2250	2350	0.18	28	0.14	26	0.18	0.36
	Weak Toppling (Zone C)	2470	2600	0.48	34	0.46	33	0.39	0.90
	Intact Rock (Zone D)	2540	2650	0.95	40	0.93	38	4.89	9.00

Table 6. Discontinuity parameters for the Huangcaoping toppling slope.

Parameter	Zone A	Zone B1	Zone B2	Zone C	Zone D	Sliding Surface
Dry friction angle (°)	25	30	32	35	42	23
Dry cohesion (MPa)	0.075	0.1	0.12	0.7	1	0.1
Saturated friction angle (°)	19.2	24.8	26.5	32.2	40.5	17.6
Saturated cohesion (MPa)	0.056	0.08	0.096	0.63	0.95	0.075
Tensile strength (MPa)	0.05	0.1	0.15	0.5	1	0
Normal stiffness (GPa/m)	10	10	15	20	30	10
Shear stiffness (GPa/m)	2	2	8	10	15	2

3. Boundary and reservoir loading conditions. The slope surface and crest were treated as free boundaries. The left and right boundaries constrained horizontal displacement, whereas the base constrained normal displacement. The reservoir was raised to 1130 m (CNVD 1985), and hydrostatic pressure was applied over the submerged extent to represent the hydraulic action. In addition, the strength parameters of discontinuities within the saturated zone were reduced by the softening factor to represent wetting-induced weakening.

4.4.2. UDEC Results

Using the strength reduction method (SRM), slope stability analyses were conducted with the UDEC model to systematically evaluate the factor of safety and the corresponding failure mode (Figure 13). The results show that, under the reservoir impoundment condition, the UDEC-derived factor of safety is 0.99, which is close to the value of 0.978 obtained using the proposed improved GB method; the discrepancy between the two is negligible. In terms of failure mechanism, the UDEC simulation depicts a typical progressive failure process governed by toe traction. Specifically, local damage initiates at the slope toe and progressively propagates upward, subsequently driving sustained displacement of the upper rock mass and leading to structural instability. Further comparison indicates that the extent of the very strongly toppled zone identified with UDEC is broadly consistent with the potential failure range delineated by the improved GB method. The two approaches mutually corroborate the inferred failure zoning and the dominant controlling sector. Overall, the improved GB method is capable of capturing the key instability features of this type of slope under reservoir conditions, producing credible results that can provide a robust basis for subsequent stability evaluation and engineering mitigation measures.

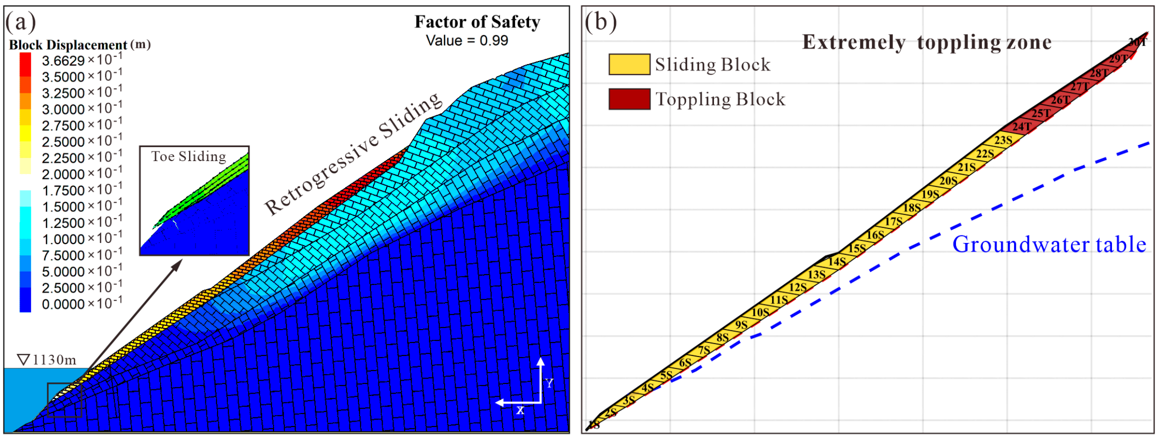

Figure 13. Comparison of failure patterns: (**a**) UDEC results; (**b**) improved GB method results.

In terms of computational efficiency and model comparison, the proposed improved GB method requires approximately 1 min for a single run, whereas the UDEC simulation requires approximately 12 h, demonstrating a clear advantage of the improved GB method in computational efficiency. Benefiting from this efficiency gain, the proposed approach enables batch calculations for multiple parameter combinations within an acceptable time cost and further facilitates Monte Carlo analyses. Compared with the distinct element method, it is therefore more convenient for systematically and comprehensively evaluating parameter uncertainty and its influence on stability outcomes.

Of note, the proposed method assumes a predefined basal slip surface and thus cannot reproduce the overall structural response and progressive failure process with the same level of detail as the distinct element method, representing a limitation. Overall, the improved GB method can serve as an effective complement to distinct element simulations. Specifically, it can be used to rapidly screen key parameters and sensitive ranges, and it provides statistically meaningful references for understanding and selecting uncertain parameters, thereby supporting subsequent high-fidelity numerical simulations and engineering decision making.

5. Discussion

5.1. Sensitivity Analysis of Failure Mode, Occurrence Probability, and Factor of Safety

As the predicted failure mode can change substantially with parameter variations, the previous chapter evaluated parameter sensitivity in terms of the factor of safety under a fixed failure mode to enable consistent comparisons. This chapter focuses on the unconstrained case, examining how parameter changes influence the failure mode, its occurrence probability, and the factor of safety associated with different modes.

As shown in Figure 14, under different parameter settings, the block composition of the governing failure mode, including sliding, toppling, and stable blocks, varies in a coupled manner with both the occurrence probability of that mode under Monte Carlo perturbations, represented by the cyan curve, and the corresponding factor of safety F_s, represented by the red curve. Overall, across the six groups of cases, sliding blocks are consistently dominant, typically numbering approximately 19–24, whereas toppling blocks generally number 5–7. The number of stable blocks varies from 0 to 13. This indicates a composite mechanism characterized by sliding dominance, toppling participation, and a variable stable segment. The occurrence probability is mostly within 0.10–0.20, suggesting that under stochastic perturbations, the governing mode is not strictly unique and that mode dispersion is present.

In detail, increasing the discontinuity connectivity ratio k promotes rapid upslope expansion of the sliding segment and a pronounced shortening of the stable segment. The factor of safety F_s decreases overall, and the occurrence probability becomes more fluctuating. This indicates that higher persistence both reduces stability and weakens the consistency of the governing mechanism. For variations in the softening coefficient, the scales of sliding and toppling remain largely unchanged. The resulting change in F_s is small, whereas the probability shows fluctuations in the intermediate range, suggesting that softening primarily intensifies competition among closely related modes. The bedding dip angle β produces a non-monotonic response in F_s. Meanwhile, the probability tends to become more concentrated as β increases, implying that changes in geometric and kinematic conditions reshape the governing mechanism through the competing effects of shear connectivity and toppling moment. As the basal friction angle φ_b increases, F_s generally increases. The block partition remains sliding-dominated, with only minor adjustments to the boundaries between block types and localized probability fluctuations. The basal cohesion c_b is the most influential parameter. With increasing c_b, the stable segment expands and the sliding segment contracts. Here, F_s increases markedly, and the probability becomes more concentrated, indicating that cohesion most directly suppresses the controlling sliding zone. The tensile strength σ_t provides only a limited increase in F_s; however, it can adjust the partition among stable, toppling, and sliding blocks and, over some ranges, increase the occurrence probability. This effect is mainly achieved by modifying boundary conditions associated with toppling or tension-controlled behavior.

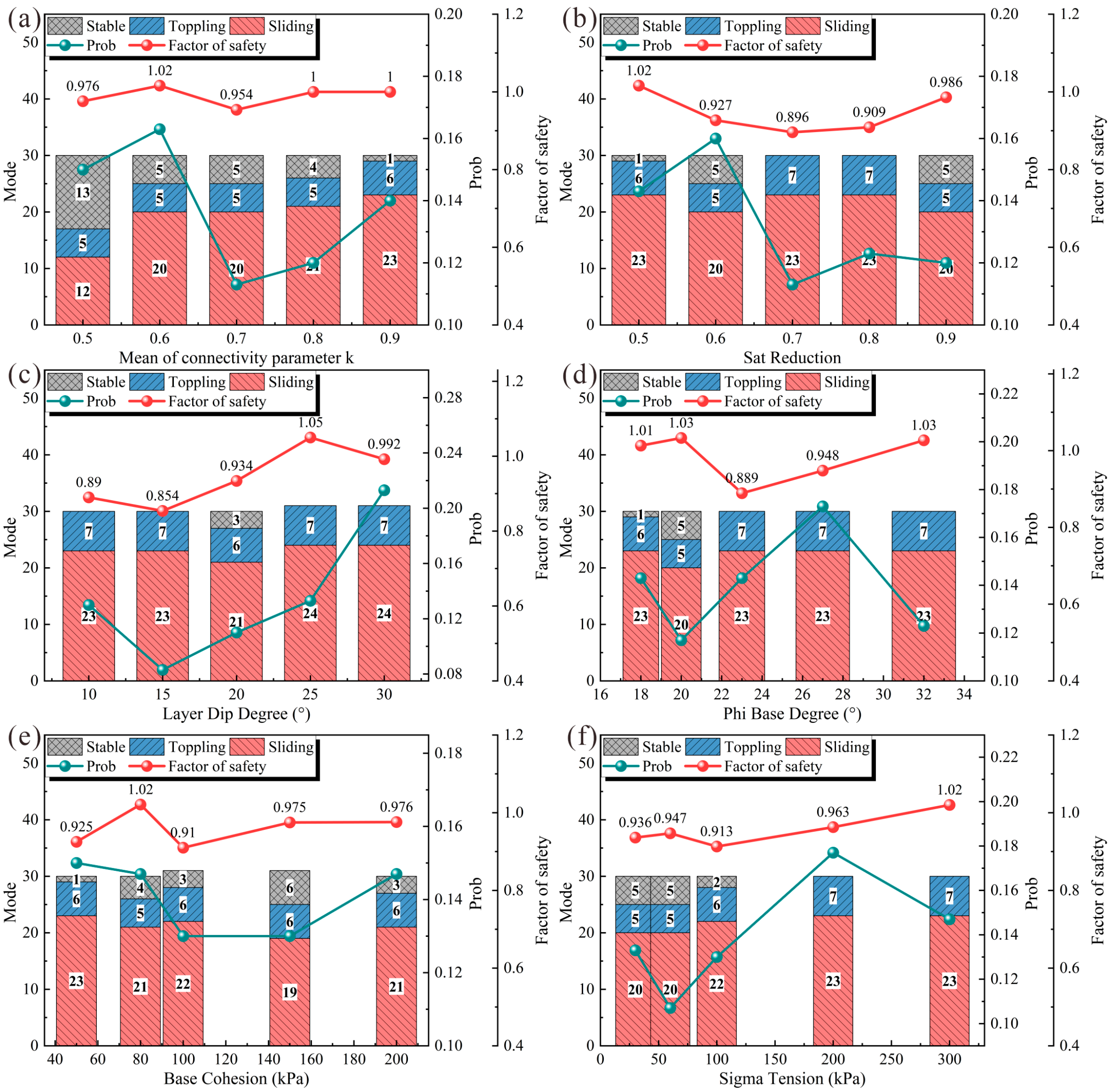

Figure 14. Coupled variations in governing failure mode composition, occurrence probability, and factor of safety F_s under parameter perturbations: (**a**) Discontinuity connectivity ratio k; (**b**) softening coefficient r_{sat}; (**c**) bedding dip angle β; (**d**) basal friction angle φ_b; (**e**) basal cohesion c_b; and (**f**) tensile strength σ_t.

Although the present framework is quasi-static and does not explicitly simulate a time-dependent triggering process, the results consistently indicate a critical initiation zone. Under reservoir impoundment, loss of equilibrium tends to occur first in the slope toe, where discontinuities are more likely to fall within the saturated zone and thus undergo wetting-induced softening. This early destabilization at the toe can subsequently promote upward deformation propagation and interact with toppling in the upper slope, suggesting that the toe acts as the primary controlling zone from an engineering perspective.

5.2. Limitations

This study evaluates slope stability under a quasi-static, limit equilibrium formulation using rate-independent strength parameters for blocks and discontinuities. Therefore, strain-rate effects and time-dependent behaviors are not explicitly captured. For slopes where long-term creep, cyclic loading, or rapid/dynamic disturbances are significant, rate-dependent/viscoplastic constitutive modeling with laboratory calibration at representative strain rates (e.g., ISOTACH-, TESRA-, or P&N-type frameworks) would be more appropriate [44–47].

The improved GB method employs an equivalently effective stress approach, consolidating pore pressure effects into unified force and friction terms. This simplification contrasts with physical reality, where pore pressure is dynamically controlled by fracture connectivity, recharge conditions, and stress-dependent hydraulic apertures. Such factors typically generate preferential seepage pathways and localized pressure peaks that vary spatiotemporally. By adopting a simplified connectivity assumption, the current framework inevitably smooths these local extremes, potentially obscuring critical seepage concentrations near the slope toe. Therefore, although effective for rapid assessment, this framework ideally serves as a precursor to more detailed coupled DEM analyses, which can rigorously account for discrete flow paths and complex stress–seepage interactions.

6. Conclusions

In summary, this study developed a probabilistic extension of the GB method for reservoir bank anti-dip rock slopes, aiming to achieve improved governing mode identification, numerical robustness, and consistency between stability evaluation and mechanism interpretation. The main conclusions are as follows:

1. An improved GB framework was established, in which the governing failure mode is identified probabilistically using Monte Carlo-based mode identification, probability weighting, and factor of safety back-calculation. A tolerance threshold was introduced to improve convergence and reduce artificial mode switching, and MaxNeg provides a stable near-critical basis for back-calculation.
2. Application to the Huangcaoping anti-dip slope at a reservoir water level of 1130 m yielded a probability-weighted mean factor of safety of approximately 0.978, indicating a near critical state. The predicted pattern revealed lower-slope sliding and upper-slope toppling, and the sliding elevation range was consistent with field observations.
3. The Monte Carlo results showed that mode switching is common, as the most frequent mode accounts for only approximately 11.7%. Failure scales were clustered into slope spanning (approximately 41.4%), mid to lower local (approximately 41.2%), and toe shallow (approximately 14.1%). The sensitivity results indicated that the basal cohesion and basal friction angle, together with the discontinuity connectivity ratio and bedding dip angle, dominate stability, whereas softening and tensile strength mainly influence mode partitioning.

Author Contributions: All authors contributed to the manuscript and discussed the results. J.C. and J.Z. (Jiawen Zhou) drafted the manuscript and were responsible for the data processing, as well as analysis and interpretation of the results. N.J. and H.L. (Haibo Li) proposed the ideas for the thesis, designed the structure, and contributed to the final revision of the thesis. Y.H., H.L. (Hongyu Luo), and J.Z. (Jieyuan Zhang) collected the on-site data. J.Z. (Jiawen Zhou) and Y.H. secured the research funding. All authors have read and agreed to the published version of the manuscript.

Funding: This research was funded by The National Natural Science Foundation of China (52379105), the China Postdoctoral Science Foundation (2025M773145), and the Sichuan Province Innovative Talent Funding Project for Postdoctoral Fellows (BX202408).

Data Availability Statement: The data presented in this study are available on request from the corresponding author due to local government regulations.

Acknowledgments: The authors would like to thank the anonymous reviewers for their time and constructive comments on our article.

Conflicts of Interest: The authors declare no conflicts of interest.

References

1. Goodman, R.E.; Bray, J.W. Toppling of rock slopes, specialty conference on rock engineering for foundations and slopes. *Am. Soc. Civ. Eng.* **1976**, *2*, 201–234.
2. Alejano, L. Considerations on failure mechanisms of rock slopes involving toppling. *IOP Conf. Ser. Earth Environ. Sci.* **2021**, *833*, 012004. [CrossRef]
3. Haghgouei, H.; Kargar, A.R.; Amini, M.; Esmaeili, K. An analytical solution for analysis of toppling-slumping failure in rock slopes. *Eng. Geol.* **2020**, *265*, 105396. [CrossRef]
4. Zheng, D.; Pan, Y.; Wang, Q.; Zhou, H.; Zheng, H.; Li, D. Evolutionary mechanisms of deep-seated toppling deformation of rock slope under different free-face conditions. *Environ. Earth Sci.* **2023**, *82*, 221. [CrossRef]
5. Ning, Y.; Tang, H.; Zhang, G.; Smith, J.V.; Zhang, B.; Shen, P.; Chen, H. A complex rockslide developed from a deep-seated toppling failure in the upper Lancang River, Southwest China. *Eng. Geol.* **2021**, *293*, 106329. [CrossRef]
6. Bowa, V.M.; Xia, Y. Stability Analyses of Jointed Rock Slopes with Counter-tilted Failure Surface Subjected to Block Toppling Failure Mechanisms. *Arab. J. Sci. Eng.* **2018**, *43*, 5315–5331. [CrossRef]
7. Zischinsky, U. Über sackungen. *Rock Mech.* **1969**, *1*, 30–52. [CrossRef]
8. Nichol, S.L.; Hungr, O.; Evans, S.G. Large-scale brittle and ductile toppling of rock slopes. *Can. Geotech. J.* **2002**, *39*, 773–788. [CrossRef]
9. Aydan, Ö.; Shimizu, Y.; Ichikawa, Y. The effective failure modes and stability of slopes in rock mass with two discontinuity sets. *Rock Mech. Rock Eng.* **1989**, *22*, 163–188. [CrossRef]
10. Zhang, J.; Chen, Z.-y.; Wang, X. Centrifuge Modeling of Rock Slopes Susceptible to Block Toppling. *Rock Mech. Rock Eng.* **2007**, *40*, 363–382. [CrossRef]
11. Gu, D.; Huang, D. A complex rock topple-rock slide failure of an anaclinal rock slope in the Wu Gorge, Yangtze River, China. *Eng. Geol.* **2016**, *208*, 165–180. [CrossRef]
12. Huang, R.; Li, W. Formation, distribution and risk control of landslides in China. *J. Rock Mech. Geotech. Eng.* **2011**, *3*, 97–116. [CrossRef]
13. Müller-Salzburg, L. The Vajont catastrophe—A personal review. *Eng. Geol.* **1987**, *24*, 423–444. [CrossRef]
14. Tang, H.; Wasowski, J.; Juang, C.H. Geohazards in the three Gorges Reservoir Area, China—Lessons learned from decades of research. *Eng. Geol.* **2019**, *261*, 105267. [CrossRef]
15. Wang, B.; Zuo, Q.; Deng, M.; Yi, Q.; Ruan, D.; Liang, Z. Study on the deformation mechanism of chair-like bedding rock landslides under the coupling effect of geological and hydrological factors. *Eng. Geol.* **2025**, *344*, 107832. [CrossRef]
16. Zhou, J.-w.; Xu, F.-g.; Yang, X.-g.; Yang, Y.-c.; Lu, P.-y. Comprehensive analyses of the initiation and landslide-generated wave processes of the 24 June 2015 Hongyanzi landslide at the Three Gorges Reservoir, China. *Landslides* **2016**, *13*, 589–601. [CrossRef]
17. Huang, D.; Gu, D.M. Influence of filling-drawdown cycles of the Three Gorges reservoir on deformation and failure behaviors of anaclinal rock slopes in the Wu Gorge. *Geomorphology* **2017**, *295*, 489–506. [CrossRef]
18. He, C.; Hu, X.; Tannant, D.D.; Tan, F.; Zhang, Y.; Zhang, H. Response of a landslide to reservoir impoundment in model tests. *Eng. Geol.* **2018**, *247*, 84–93. [CrossRef]
19. Miao, F.; Wu, Y.; Li, L.; Tang, H.; Xiong, F. Weakening laws of slip zone soils during wetting–drying cycles based on fractal theory: A case study in the Three Gorges Reservoir (China). *Acta Geotech.* **2020**, *15*, 1909–1923. [CrossRef]
20. Huang, D.; Gu, D.M.; Song, Y.X.; Cen, D.F.; Zeng, B. Towards a complete understanding of the triggering mechanism of a large reactivated landslide in the Three Gorges Reservoir. *Eng. Geol.* **2018**, *238*, 36–51. [CrossRef]
21. Xie, J.; Uchimura, T.; Huang, C.; Maqsood, Z.; Tian, J. Experimental Study on the Relationship between the Velocity of Surface Movements and Tilting Rate in Pre-Failure Stage of Rainfall-Induced Landslides. *Sensors* **2021**, *21*, 5988. [CrossRef] [PubMed]
22. Song, K.; Wang, F.; Yi, Q.; Lu, S. Landslide deformation behavior influenced by water level fluctuations of the Three Gorges Reservoir (China). *Eng. Geol.* **2018**, *247*, 58–68. [CrossRef]
23. Gu, D.; Liu, H.; Gao, X.; Huang, D.; Zhang, W. Influence of Cyclic Wetting–Drying on the Shear Strength of Limestone with a Soft Interlayer. *Rock Mech. Rock Eng.* **2021**, *54*, 4369–4378. [CrossRef]
24. Beng, X.; Zhang, G.; Yang, Y.; Zhu, C.; Karakus, M.; Wang, D. Flexural toppling characteristics of anti-dip soft rock slope with base friction test. *Bull. Eng. Geol. Environ.* **2022**, *82*, 21. [CrossRef]
25. Liu, G.; Li, J.; Kang, F. Failure Mechanisms of Toppling Rock Slopes Using a Three-Dimensional Discontinuous Deformation Analysis Method. *Rock Mech. Rock Eng.* **2019**, *52*, 3825–3848. [CrossRef]

26. Zhang, B.; Fang, K.; Tang, H.; Sumi, S.; Ding, B. Block-flexure toppling in an anaclinal rock slope based on multi-field monitoring. *Eng. Geol.* **2023**, *327*, 107340. [CrossRef]
27. Bray, J.W.; Goodman, R.E. The theory of base friction models. *Int. J. Rock Mech. Min. Sci. Geomech. Abstr.* **1981**, *18*, 453–468. [CrossRef]
28. Sarma, S. Stability Analysis of Embankments and Slopes. *Geotech. Eng. Div. ASCE* **1979**, *105*, 1511. [CrossRef]
29. Wyllie, D.C. Toppling rock slope failures examples of analysis and stabilization. *Rock Mech.* **1980**, *13*, 89–98. [CrossRef]
30. Zanbak, C. Design Charts for Rock Slopes Susceptible to Toppling. *J. Geotech. Eng.* **1983**, *109*, 1039–1062. [CrossRef]
31. Sagaseta, C.; Sánchez, J.M.; Cañizal, J. A general analytical solution for the required anchor force in rock slopes with toppling failure. *Int. J. Rock Mech. Min. Sci.* **2001**, *38*, 421–435. [CrossRef]
32. Chaudhary, N.; Shubham, K.; Metya, S.; Sharma, K.K. Analytical and predictive assessment of rounding effects on rock slope stability under block toppling using adaptive moment estimation optimization. *Model. Earth Syst. Environ.* **2025**, *11*, 340. [CrossRef]
33. Azarafza, M.; Akgün, H.; Ghazifard, A.; Asghari-Kaljahi, E. Key-block based analytical stability method for discontinuous rock slope subjected to toppling failure. *Comput. Geotech.* **2020**, *124*, 103620. [CrossRef]
34. Chen, Z.; Gong, W.; Ma, G.; Wang, J.; He, L.; Xing, Y.; Xing, J. Comparisons between centrifuge and numerical modeling results for slope toppling failure. *Sci. China Technol. Sci.* **2015**, *58*, 1497–1508. [CrossRef]
35. Xie, J.; Uchimura, T.; Wang, G.; Selvarajah, H.; Maqsood, Z.; Shen, Q.; Mei, G.; Qiao, S. Predicting the sliding behavior of rotational landslides based on the tilting measurement of the slope surface. *Eng. Geol.* **2020**, *269*, 105554. [CrossRef]
36. Xie, J.; Uchimura, T.; Wang, G.; Shen, Q.; Maqsood, Z.; Xie, C.; Liu, J.; Lei, W.; Tao, S.; Chen, P.; et al. A new prediction method for the occurrence of landslides based on the time history of tilting of the slope surface. *Landslides* **2020**, *17*, 301–312. [CrossRef]
37. Wang, W.; Li, Z.; Du, F.; Cao, Z.; Shi, J.; Zhai, M.; Liu, M. Study on the evolution law of failure depth of large mining height and ultra-wide working surface. *Sci. Rep.* **2026**, *16*, 665. [CrossRef]
38. Yangbo, D.; Yushan, M.; Zhenghao, Y.; Song, C.; Zinan, L. Reservoir Region Anti-dip Slope Stability Assessment Based on Modified Goodman–Bray Method. *Coal Geol. China* **2020**, *32*, 62–66. (In Chinese) [CrossRef]
39. Duan, L. Study on Relationship Between Deformation Characteristics and Reservoir Water Level Change of Huangcaoping Toppling Deformation Slope. Master's Thesis, Chengdu University of Technology, Chengdu, China, 2021. [CrossRef]
40. Zhang, H.; Xu, X.; Zheng, Y.; Li, H.; Guo, H. Experimental and numerical study of the mechanism of block–flexure toppling failure in rock slopes. *Bull. Eng. Geol. Environ.* **2022**, *81*, 63. [CrossRef]
41. Zhu, D.; Griffiths, D.V.; Fenton, G.A.; Huang, J. Probabilistic stability analyses of two-layer undrained slopes. *Comput. Geotech.* **2025**, *182*, 107178. [CrossRef]
42. Sarfaraz, H.; Amini, M. Numerical Simulation of Slide-Toe-Toppling Failure Using Distinct Element Method and Finite Element Method. *Geotech. Geol. Eng.* **2020**, *38*, 2199–2212. [CrossRef]
43. Lee, J.; Kim, K.-I.; Min, K.-B.; Rutqvist, J. TOUGH-UDEC: A simulator for coupled multiphase fluid flows, heat transfers and discontinuous deformations in fractured porous media. *Comput. Geosci.* **2019**, *126*, 120–130. [CrossRef]
44. Xie, J.; Chen, J.; Maqsood, Z.; Li, K.; Zhao, S.; Fang, K. Influences of stress on time-dependent behaviors and failure estimation: Insights from creep tests and dynamic loading tests. *Bull. Eng. Geol. Environ.* **2025**, *85*, 7. [CrossRef]
45. Shaikh, M.; Kyokawa, H.; Maqsood, Z.; Ahsan, M.K.; Koseki, J. Mechanical behaviour and loading rate dependency of gypsum-mixed fine-grained soils. *Proc. Inst. Civ. Eng. Geotech. Eng.* **2021**, *176*, 166–177. [CrossRef]
46. Maqsood, Z.; Koseki, J.; Miyashita, Y.; Xie, J.; Kyokawa, H. Experimental study on the mechanical behaviour of bounded geomaterials under creep and cyclic loading considering effects of instantaneous strain rates. *Eng. Geol.* **2020**, *276*, 105774. [CrossRef]
47. Maqsood, Z.; Koseki, J.; Ahsan, M.K.; Shaikh, M.; Kyokawa, H. Experimental study on hardening characteristics and loading rate dependent mechanical behaviour of gypsum mixed sand. *Constr. Build. Mater.* **2020**, *262*, 119992. [CrossRef]